



Stabilizing Zn/electrolyte Interphasial Chemistry by a Sustained-Release Drug Inspired Indium-Chelated Resin Protective Layer for High-Areal-Capacity Zn//V₂O₅ Batteries

Minghao Zhang, Siyang Li, Rong Tang, Chenxi Sun, Jin Yang, Guanhong Chen, Yuanhong Kang, Zeheng Lv, Zhipeng Wen, Cheng Chao Li,* Jinbao Zhao,* and Yang Yang*

Abstract: For zinc-metal batteries, the instable chemistry at Zn/electrolyte interphasial region results in severe hydrogen evolution reaction (HER) and dendrite growth, significantly impairing Zn anode reversibility. Moreover, an often-overlooked aspect is this instability can be further exacerbated by the interaction with dissolved cathode species in full batteries. Here, inspired by sustained-release drug technology, an indium-chelated resin protective layer (Chelex-In), incorporating a sustained-release mechanism for indium, is developed on Zn surface, stabilizing the anode/electrolyte interphase to ensure reversible Zn plating/stripping performance throughout the entire lifespan of Zn//V₂O₅ batteries. The sustained-release indium onto Zn electrode promotes a persistent anticatalytic effect against HER and fosters uniform heterogeneous Zn nucleation. Meanwhile, on the electrolyte side, the residual resin matrix with immobilized iminodiacetates anions can also repel detrimental anions (SO₄²⁻ and polyoxovanadate ions dissolved from V₂O₅ cathode) outside the electric double layer. This dual synergetic regulation on both electrode and electrolyte sides culminates a more stable interphasial environment, effectively enhancing Zn anode reversibility in practical high-areal-capacity full battery systems. Consequently, the bio-inspired Chelex-In protective layer enables an ultralong lifespan of Zn anode over 2800 h, which is also successfully demonstrated in ultrahigh areal capacity Zn//V₂O₅ full batteries (4.79 mAh cm⁻²).

Introduction

The rapid development of renewable energy has spurred a thriving market for grid-scale electrochemical energy storage.^[1] However, the frequent occurrence of safety incidents has raised public concerns about energy storage systems that rely on flammable organic electrolytes, such as lithium-ion batteries.^[2] Benefitting from the intrinsic safety of aqueous electrolyte and the advantages of Zn metal anodes, including high capacity (820 mAh g⁻¹), low potential (−0.76 V, vs. SHE), and natural abundance, rechargeable aqueous zinc metal batteries (AZMBs) are emerging as one of the most promising candidates for the next generation large-scale energy storage technology.^[3] However, the volatile chemical environment at the Zn/electrolyte interphase, characterized by the high reactivity of aqueous electrolytes and uncontrollable Zn nucleation and deposition, can trigger dendrite growth, hydrogen evolution reactions (HER), and the accumulation of inert basic zinc salt by-products (like Zn₄SO₄(OH)₆·xH₂O, ZSH, in ZnSO₄ electrolyte), significantly impeding the commercialization of AZMBs.^[4]

According to the typical electrochemical model, the Zn/electrolyte interphasial region is composed of both metallic Zn electrode phase and liquid electrolyte phase.^[5] And Zn electrodeposition is a multifaceted electrochemical process that involves mass transfer and desolvation in the electrolyte phase, alongside nucleation and crystal growth in the electrode phase.^[6] Within the electrolyte phase, solvent water molecules, particularly those in the solvation shell of [Zn(H₂O)₆]²⁺, are highly susceptible to electro-reduction due to their thermodynamic instability during zinc electrodeposition,^[7] thereby exacerbating risk of HER and the subsequent by-product accumulation (Figure 1b).^[8] Encouragingly, creating a protective layer on the surface of Zn can effectively diminish the presence of active interfacial H₂O, enhancing the reversibility of Zn anodes.^[9] Moreover, some meticulously designed surface coatings have been further demonstrated to facilitate Zn²⁺ ion conduction, consequently mitigating Zn dendrite growth to a certain extent.^[8a,10] However, these artificial protective layers typically do not influence the nucleation process within the electrode phase, which is critical for uniform Zn deposition.^[11] Generally, due to the absence of the nucleation sites on pristine Zn foils, “homogeneous nucleation” on Zn sites requires a higher degree of supersaturation than heterogeneous nucleation, necessitating a larger overpoten-

[*] M. Zhang, S. Li, R. Tang, C. Sun, J. Yang, G. Chen, Y. Kang, Z. Lv, Prof. J. Zhao, Dr. Y. Yang
 State Key Lab of Physical Chemistry of Solid Surfaces, State-Province Joint Engineering Laboratory of Power Source Technology for New Energy Vehicle, College of Chemistry and Chemical Engineering, Xiamen University, Xiamen, 361005, P. R. China
 E-mail: jbzha@xmu.edu.cn
 yangyang419@xmu.edu.cn
 Dr. Z. Wen, Prof. C. C. Li
 School of Chemical Engineering and Light Industry, Guangdong University of Technology, Guangzhou 510006, P. R. China
 E-mail: licc@gdut.edu.cn

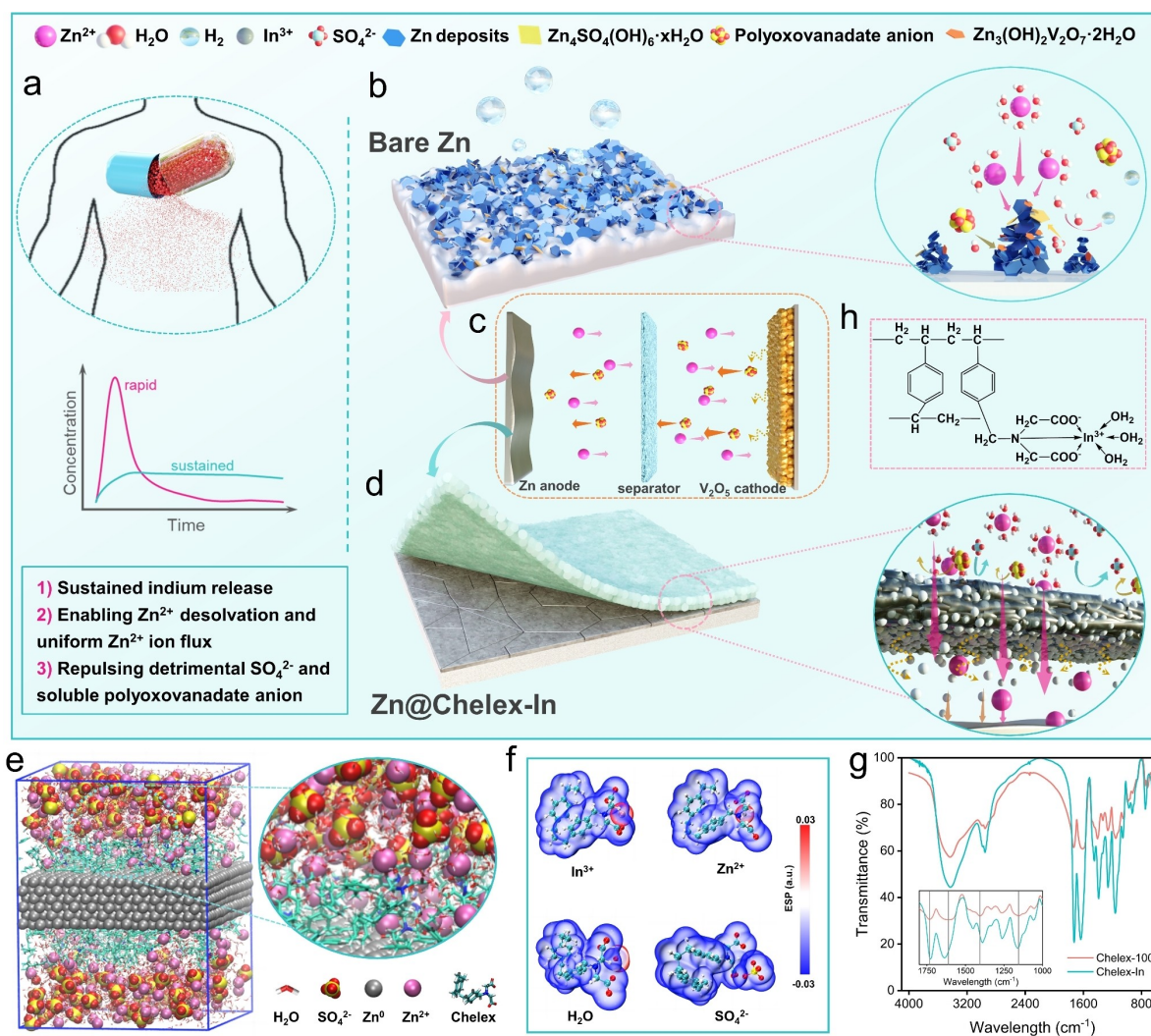


Figure 1. (a–d) Schematic diagram of (a) sustained-release drug, (b) deterioration of bare Zn anode, (c) dissolution and shuttle of detrimental soluble polyoxovanadate anion from V₂O₅ cathode, and (d) enhanced Zn deposition by Chelex-In. (e) The snapshot of interphasial region that Zn@Chelex-In in 2 M ZnSO₄ electrolyte obtained by molecular dynamics (MD) simulations. (f) The electrostatic potential (ESP) isosurface plots between Chelex and In³⁺, Zn²⁺, H₂O and SO₄²⁻. (g) FTIR spectra of Chelex-100 and Chelex-In. (h) The Structural formula of Chelex-In.

tial for electrodeposition.^[12] Besides, the surface of commercial zinc foil is not uniformly smooth, leading to electrodeposition preferentially occurring at surface defects like bumps or scratches to minimize the interface energy, resulting in uncontrolled Zn nucleation and growth.^[13] Recently, the employment of zincophilic metals (e.g., Ni, Cu, Ag, Sn, Bi, Sb, etc.)^[14] on Zn anode surface has been recognized for promoting favorable heterogeneous nucleation, achieving uniform nucleation of the initial deposition process. Nevertheless, the effectiveness of such metals may be limited due to the obscuring of these metals by Zn deposition under high areal capacity conditions.^[13a,15] Hence, reconciling Zn nucleation and mass transfer behavior in the electrode/electrolyte interphase enduringly is crucial for the long-term cycling stability of Zn anodes.

It is also noteworthy that the reported lifespan of Zn metal anodes in full cells (calculated by the cumulative capacity of Zn) is usually inferior to that in symmetric cells

(Figure S1 and Table S1). This discrepancy may be related to the interference of dissolved cathode species on the Zn anode side, particularly under high-areal-capacity conditions. Taking representative Zn//V₂O₅ battery system for an example, we found that V₂O₅ cathode is partially dissolved and transformed to soluble anionic decavanadate in the bulk electrolyte during cycling, which can transfer to the anode side and eventually deposit on the Zn surface as insoluble Zn₃(OH)₂V₂O₇·2H₂O, (ZVO). These irreversible by-products are prone to disturb Zn²⁺ transport and increase the interfacial polarization, resulting in an accelerated risk of internal short circuits (Figure 1b,c). Therefore, it is also significant to prevent the crosstalk of dissolved cathode species to avoid the unsatisfactory effects of Zn metal anode modification strategies in practical full batteries.^[3b,16]

Sustained-release drugs are dosage forms designed to release active ingredients at a predetermined rate, aiming to prolong their therapeutic effects over an extended period,

which have been extensively adopted for the treatment of chronic diseases (Figure 1a). Inspired by this, an indium-chelated resin protective layer (Chelex-In) with the functionality of sustained-release indium is designed on the surface of Zn anode, realizing the stabilization of both electrode and electrolyte sides of the interphasial region throughout the entire lifespan of Zn//V₂O₅ batteries. This protective layer enables the sustained release of In³⁺ from the resin, which is then electro-reduced on the electrode surface. This process not only provides continuous heterogeneous nucleation sites for Zn deposition but also alleviates HER side reactions based on the inherent HER anticatalytic features of indium. Furthermore, the anchored resin matrix layer can repel detrimental anions, meanwhile regulating the solvation structure of zinc ions, mitigating erosion and smoothening mass transfer in the electrolyte (Figure 1c–e). In the practical Zn//V₂O₅ full battery system, the Chelex-In is demonstrated to effectively impede the shuttle of decavanadate and prevent the formation of inert ZVO on the anode, thus circumventing serious dendrite growth under high-areal-capacity conditions. With the multifunctional protection of Chelex-In layer, the cyclic life of symmetric cell is extended to 2800 h with a high Coulombic efficiency of 99.85%. Moreover, the assembled Zn@Chelex-In//V₂O₅ full cells can deliver an ultrahigh area capacity of 4.79 mAh cm⁻² over 200 stable cycles at a low N/P ratio of 3.08, validating its reliability and practicality.

Results and Discussion

The Verification of Sustained Indium Release

The Chelex-In is prepared through an ion exchange route between commercial Chelex-100 chelating resin and In³⁺, which is subsequently coated onto commercial Zn foils to obtain the Zn@Chelex-In electrodes, and the thickness of resin layer is around 15 μm (Figure S2). Chelex-100 chelating resin is composed of the polystyrene-divinylbenzene containing iminodiacetate (IDA) groups, which can form a chelate (complex) with high-valence cations like In³⁺ and Zn²⁺.^[17] Electrostatic potential (ESP) calculation results (Figure 1f) show that IDA groups in Chelex are surrounded by negative charges, enhancing their affinity for In³⁺ cations. Besides, Fourier transform infrared spectroscopy (FTIR) analysis (Figure 1g) reveals the shift of peaks at 1732 cm⁻¹, 1611 cm⁻¹, and 1406 cm⁻¹ after ion exchange, signifying the coordination of carboxyl groups with In³⁺. The appearance of a new peak at 1451 cm⁻¹ and the shift at 1155 cm⁻¹ are assigned to the involvement of N atoms in coordinating with In³⁺.^[18] Consequently, the imino and carboxyl groups in IDA can act as tridentate ligands for chelating In³⁺ (Figure 1h),^[19] effectively anchoring it within the resin layer. It can be seen that the Chelex-In protective layer is uniform and smooth with a homogeneous distribution of indium element (Figure S3).

Through a typical ion-exchange method, the selectivity coefficient of Chelex-100 chelating resin towards In³⁺ and Zn²⁺ is measured to be notably high at 400:1 (Table S2).

The low-valence Zn²⁺ cations with a high concentration in the bulk electrolyte, are expected to compete with In³⁺ for coordination sites, realizing the sustained release of In³⁺ from the resin. Meanwhile, the existence of an electric field in battery may also promote the release of In³⁺, which is monitored using an H-type electrolytic cell (Figure 2a,b). Given the lower reduction potential of Zn²⁺ (−0.762 V vs. SHE) compared to that of In³⁺ (−0.338 V vs. SHE), a moderate constant potential of −0.45 V (vs. Ag/AgCl) is applied to the platinum working electrode to establish an electric field through water electrolysis while preventing the reduction of In³⁺ in the electrolyte. And the amount of released indium ions is quantified by the inductively coupled plasma optical emission spectrometer (ICP-OES). Notably, the concentration of In³⁺ increases slowly without electric field, underscoring the weak competition from low-valence cations. However, upon the application of an electric field, both the concentration and the releasing rate of In³⁺ are significantly increased, revealing that the existence of electric field can indeed expedite the release of In³⁺ from Chelex-In. Furthermore, the finite element simulation is employed to visually assess the impact of electric field on indium release more intuitively. As presented in Figure 2c, the existence of electric field results in a higher concentration and a more uniform distribution of released In³⁺ within the electrolyte. This electric field induces the electromigration of In³⁺, improving its transport and diminishing the diffusion-induced concentration gradient. Moreover, the diminished In³⁺ concentration at the interphase can also promote the chelation equilibrium towards dissociation, thereby expediting the indium release.

To get deeper insights into the release and deposition behavior of In³⁺ under the influence of electric fields in batteries, the electrochemical quartz crystal microbalance with dissipation monitoring (EQCM–D) is conducted (Figure 2d,e). Herein, a Na₂SO₄ solution is selected to eliminate the interference caused by Zn deposition and dissolution. Cyclic voltammetry (CV) measurement is performed within the range of 0.7 V to −0.7 V (vs. Ag/AgCl) to ensure the occurrence of a complete indium redox reaction. Initially, the EQCM–D test is conducted on a bare Au quartz electrode to evaluate the impact of electrolyte. As shown in Figure 2d, the substantial reduction current coupled with a negligible oxidation current indicates the occurrence of HER on the electrode, while the minimal changes in mass and dissipation during CV scanning are attributed to the exchange between proton and adsorbed water molecules at the interface.^[20] By comparison, the periodic and evident mass variation on the Au@Chelex-In electrode during CV scanning indicates the release of In³⁺ from the resin layer as well as its reversible dissolution and deposition on the Au quartz electrode. Besides, the Faraday current is still predominantly contributed by the HER, as inferred from the significantly higher reduction current relative to the oxidation current. Meanwhile, experiments with zinc-chelated resin (Chelex-Zn) are also conducted to exclude the potential influence of the resin matrix itself. Apparently, the mass change observed with Au@Chelex-Zn is significantly lower than that with Au@Chelex-In, confirming the obvious

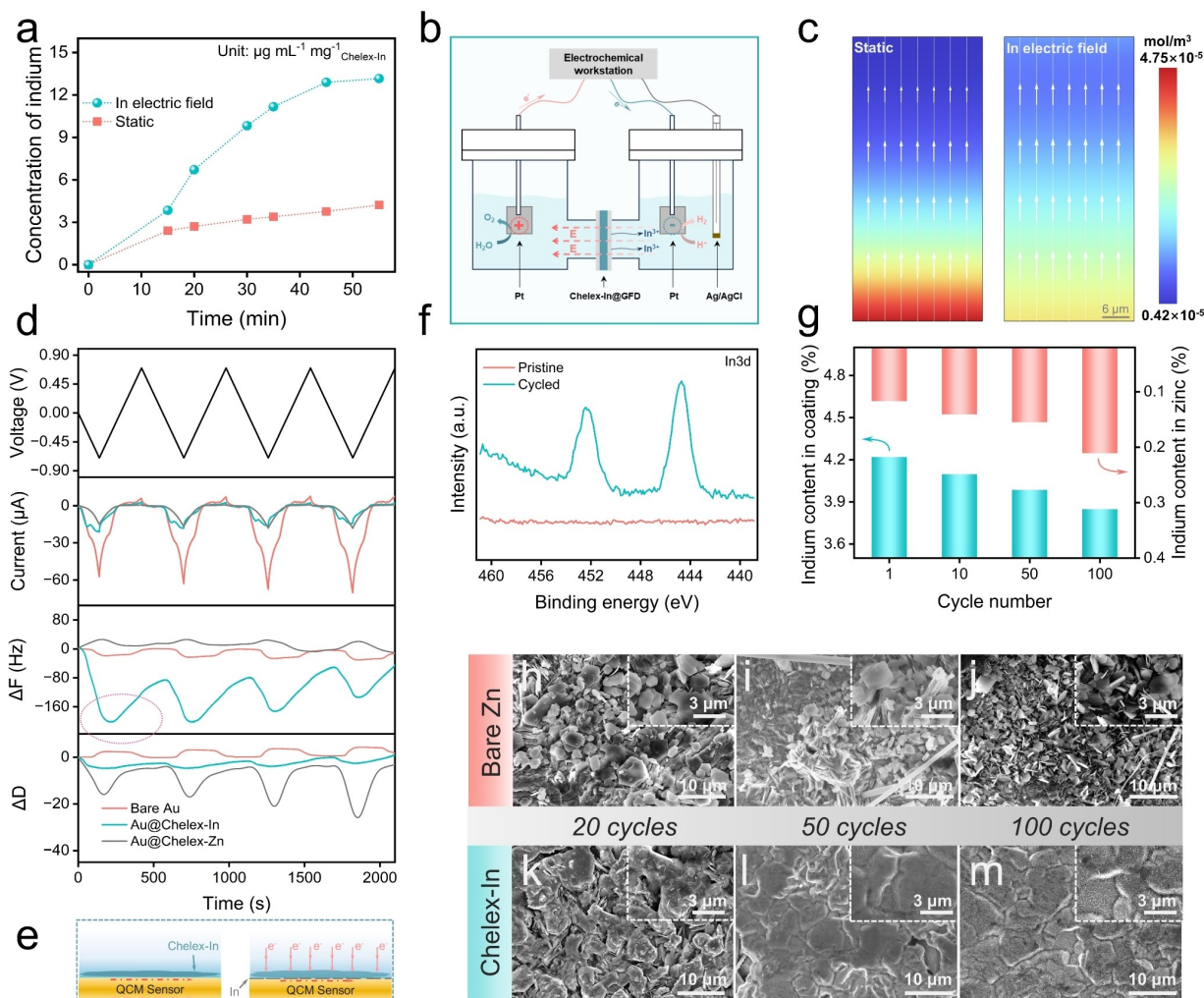


Figure 2. (a) The concentration of In^{3+} released from Chelex-In over different times through ICP-OES, and (b) the corresponding schematic diagram of the experimental device. (c) The distribution of In^{3+} at Chelex-In/electrolyte interphase through COMSOL Multiphysics. (d) The time-voltage/current/frequency-change/dissipation-change curve on different quartz electrodes through EQCM-D, and (e) corresponding schematic diagram of the changing process for Au@Chelex-In. (f) XPS spectra of pristine Zn and cycled Zn@Chelex-In (the resin layer is removed). (g) The indium content in cycled electrodes and corresponding resin layers after different cycles (obtained by ICP-OES). (h–m) The scanning electron microscope (SEM) images of bare Zn electrodes after (h) 20 cycles, (i) 50 cycles and (j) 100 cycles, and Zn@Chelex-In electrodes after (k) 20 cycles, (l) 50 cycles and (m) 100 cycles. The cycled electrodes aforementioned are cycled at 1 mA cm^{-2} for 1 mAh cm^{-2} , and generally 50 cycles unless separate annotation.

mass variation for the Au@Chelex-In electrode is indium-related. Besides, the Au@Chelex-Zn exhibits a more pronounced change in dissipation, which can be ascribed to the morphological alteration induced by water molecule migration within the resin.

Based on the above investigation, it can be inferred that In^{3+} ions in the Chelex-In layer will be sustainably extruded and co-deposited with Zn^{2+} onto Zn anodes during the plating process. X-ray photoelectron spectroscopy (XPS) analysis of the cycled Zn@Chelex-In electrode surface after removing the upper Chelex-In layer clearly shows the presence of indium (Figure 2f). Moreover, as the cycle number increases, the indium content in the Chelex-In layer decreases, while that in the Zn electrode increases continuously (Figure 2g), indicating a progressive accumulation of indium in the zinc deposition layer. Considering the

inevitable increase of reaction area in Zn electrodes during cycling, such a sustained indium release effect is of great importance, which can be reflected in the morphology evolution of zinc deposits. As shown in (Figure 2h–j), the surfaces of cycled bare Zn electrodes exhibit an aggregation of fragmented zinc deposits, which becomes more severe after repeated cycling. In contrast, the Chelex-In protected electrodes not only show a distinct reduction of fragmented deposits but also demonstrate a unique “self-healing” feature where the Zn deposition layer becomes increasingly smooth over successive cycles (Figure 2k–m). This self-healing effect may be due to the rising indium content in the deposited layer, which exerts a stronger regulation ability on deposition behavior.

The Stable Interphasial Chemistry Enabled by Sustained-release Indium and Anchored Resin Matrix

During the electroreduction process, a high energy barrier must be overcome for $[\text{Zn}(\text{H}_2\text{O})_6]^{2+}$ to shed their solvation sheath water molecules before transitioning to Zn^0 .^[21] These unstable water molecules are prone to be reduced on the electrode surface, leading to the production of H_2 and ZSH. Notably, according to the ESP results in Figure 1f, the IDA groups in Chelex resin can also attract Zn^{2+} while repelling SO_4^{2-} in the bulk electrolyte, highlighting its potential to modulate the solvation structure of $[\text{Zn}(\text{H}_2\text{O})_6]^{2+}$. As a critical rate-controlled step in the electro-reduction of Zn^{2+} , the desolvation process is reflected in the interface activation energy (E_a), which can be calculated using the Arrhenius equation (equation 1).^[22] In this equation, R_{ct} is the interfacial resistance (measured via electrochemical impedance spectroscopy (EIS)), A is the preexponential factor, R is the gas constant, and T is the thermodynamic temperature. As depicted in Figure 3a and Figure S4, the presence of Chelex layer lowers the E_a from $59.53 \text{ kJ mol}^{-1}$ to $42.90 \text{ kJ mol}^{-1}$, indicating that the Chelex resin can

effectively facilitate the desolvation process of $[\text{Zn}(\text{H}_2\text{O})_6]^{2+}$.

$$\frac{1}{R_{\text{ct}}} = A \exp(-E_a/RT) \quad (1)$$

In order to further comprehend the intrinsic mechanisms underlying the diverse desolvation behaviors, the radial distribution function (RDF) is derived from MD simulations to elucidate the coordination state of Zn^{2+} in different environments. In a pure ZnSO_4 aqueous solution, Zn^{2+} is observed to be coordinated with 6 H_2O (Figure S5), aligning with its well-known coordination structure.^[23] Due to the strong interaction between Zn^{2+} and IDA group, two H_2O in the solvation shell of $[\text{Zn}(\text{H}_2\text{O})_6]^{2+}$ are successfully replaced by one IDA group, leading to the formation of IDA- $\text{Zn}^{2+}(\text{H}_2\text{O})_4$ solvation structure (Figure 3b). Consequently, this coordination of IDA is calculated to significantly reduce the desolvation energy of hydrated zinc ions (Figure 3c), corroborating corresponding experimental results. Moreover, dynamic distribution snapshots reveal that Zn^{2+} ions are drawn closer to Chelex distinctly after 5 ns

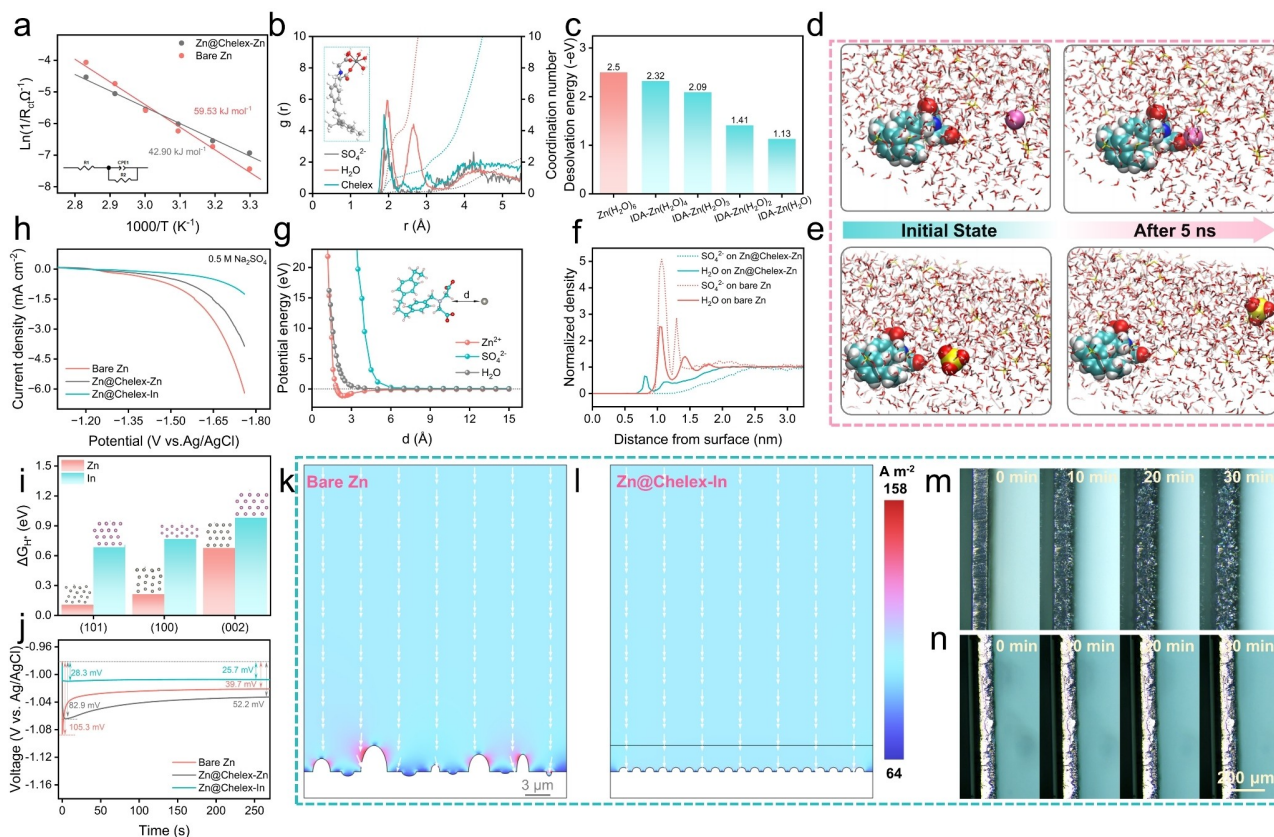


Figure 3. (a) The E_a of different electrodes calculated by the Arrhenius equation. (b) The RDF of species in the solvation sheath of Zn^{2+} with the existence of Chelex. (c) The desolvation energy barriers of Zn^{2+} coordinated in different forms. (d–e) The snapshots of dynamic interactions between Chelex and (d) Zn^{2+} or (e) SO_4^{2-} . (f) The normalized density distribution of H_2O and SO_4^{2-} on different electrodes. (g) The potential energy of IDA group in Chelex interacting with various species. (h) The LSV curves of different electrodes in $0.5 \text{ M Na}_2\text{SO}_4$ electrolyte. (i) The ΔG_{Hr} on different crystal faces obtained by DFT calculations. (j) The chronopotentiometry curves of different electrodes in 2 M ZnSO_4 electrolyte at a current density of -1 mA cm^{-2} . (k–l) The current density distributions in anode/electrolyte interphase for (k) bare Zn and (l) Zn@Chelex-In , which are obtained by finite element simulations. (m–n) In situ optical micrographs of (m) Bare Zn and (n) Zn@Chelex-In during Zn electrodeposition process at a current density of 5 mA cm^{-2} .

(Figure 3d), visualizing the strong attraction of Chelex to Zn^{2+} .

MD simulations also provide insightful details about the impact of the Chelex resin layer on other interfacial species (H_2O and SO_4^{2-}), crucial for understanding its effectiveness in mitigating side reactions and enhancing zinc anode reversibility. In the Zn/ZnSO_4 interface without modification, a random distribution of H_2O and SO_4^{2-} ions is observed (Figure S6), which will easily exacerbate HER and by-product formation.^[24] However, with the introduction of the Chelex layer, there is a noticeable reduction in the presence of these two detrimental species at the interface (Figure 1e). In addition, the dynamic distribution demonstrates that SO_4^{2-} gets far from Chelex spontaneously (Figure 3e), which coincides with the ESP results. Meanwhile, the normalized density through MD simulations (Figure 3f), also confirms the significant decrease in H_2O and SO_4^{2-} amount due to the Chelex layer intervention, illustrating its role in suppressing side reactions during cycling. Besides, the potential energy between IDA group and other species is also calculated to clarify their interactions. As illustrated in Figure 3g, the potential energy between Zn^{2+} and IDA group approaches to minimum at around 2.3 Å, and remains negative as the distance increases. In contrast, the potential energies between IDA group and SO_4^{2-} are always positive, underscoring the functionality of Chelex in attracting Zn^{2+} while repelling SO_4^{2-} . These individually targeted attraction and repulsion effects effectively reduce HER, as evidenced by linear sweep voltammetry (LSV) curves and corroborated by EQCM test and simulation results (Figure 3h). In addition, it is worth noting that the HER current is further decreased for the Chelex-In compared to the Chelex-Zn layer, indicating that the sustained indium release is helpful in suppressing the HER. According to the volcano plot,^[25] the rate-limiting step for HER on both indium and zinc metal surfaces is the adsorption process of protons or water molecules.^[26] Therefore, the density functional theory (DFT) simulation is performed to measure the Gibbs free energy of hydrogen adsorption (ΔG_{H^*}) on different metals. As presented in Figure 3i, the ΔG_{H^*} on each crystal face of indium is higher than zinc, indicating the thermodynamically hindered hydrogen adsorption process. This validates the excellent anti-catalytic effect of indium, supporting its addition in enhancing the cycling stability of Zn anodes.

Despite the excellent ions and H_2O reconfiguration enabled by the Chelex protective layer, the nature of electrode surface itself also influences Zn deposition behavior. Apparently, the simple Chelex-Zn protective layer fails to change the nature of “homogeneous nucleation” that zinc ions are reduced on the surface of metallic zinc, which requires a high overpotential during the electrodeposition process. Typically, although the zinc deposition layer is relatively flatter due to the modification of Chelex-Zn (Figure S7), some conglomerate lamellar deposits can be still detected on the Zn surface.^[27] For the Zn@Chelex-Zn electrode, instead of improving nucleation overpotential (Figure 3j), the deposition overpotential even increases due to the heightened mass transfer resistance.^[28] Moreover, as

presented in the finite element simulation (Figure 3k), due to the absence of nucleation sites and uncontrolled Zn^{2+} diffusion, zinc ion fluxes are concentrated at edges of scratches and bumps to minimize the interfacial energy,^[13b] which will further aggravate surface heterogeneity. Encouragingly, both the nucleation overpotential and the deposition overpotential are significantly reduced through the introduction of Chelex-In layer (Figure 3j). The higher electrode potential of indium facilitates its preferential deposition, and the sustained-release effect maintains continuous indium electrodeposition, providing consistent heterogeneous nucleation sites for uniform zinc deposition. And the improved wettability also contributes to the reduction of overpotential (Figure S8). On the one hand, the transfer barrier of zinc from indium is reduced (Figure S9) due to their proper binding and the less absorption of H on indium.^[29] Additionally, electrons from external circuits tend to be aggregated on the surface of indium due to its higher electrode potential, thus realizing the induction of zinc deposition.^[29a] Benefitting from the induction of Zn deposition by the heterogeneous indium nuclei and the regulation of Zn^{2+} transfer by the Chelex resin layer, the Zn^{2+} flux is remarkably uniform on the surface of Zn@Chelex-In (Figure 3l). As presented in situ optical microscopy tests (Figure 3m and Video S1), many particles appear on the surface of bare Zn at the beginning of Zn deposition, grow randomly, and arrange irregularly subsequently, which finally become a deposition layer consisting of disorder particles. For Zn@Chelex-In (Figure 3n and Video S2), the zinc is observed to be deposited below the resin on the surface, which proves that the Chelex-In layer can efficaciously restrain the growth of zinc dendrites.

Symmetric cells were assembled to evaluate the protection effect of the resin layer on zinc anode stability. The Zn//Zn symmetric cell initially exhibits a great polarization and encounters an internal short-circuit within 80 hours due to pronounced dendrite growth (Figure 4a). However, the introduction of the Chelex-Zn layer extends the cell's lifespan to 900 hours. Remarkably, the Zn@Chelex-In//Zn@Chelex-In symmetric cell achieves an ultralong lifespan of 2800 hours with a significantly reduced voltage hysteresis of only 19 mV. This notable improvement, including the gradual decrease in voltage hysteresis during cycling, highlights the continuous release and deposition of indium within the deposition layer. Besides, even under a high current density of 25 mA cm^{-2} , the Zn@Chelex-In//Zn@Chelex-In symmetric cell can also maintain stable cycling for 300 h (Figure S10). In addition, the Zn//Cu half cells are assembled to evaluate the effect of resin layer on the reversibility of zinc deposition. As shown in Figure 4b, the bare Zn//Cu half cell exhibits a distinct efficiency fluctuation after 140 cycles and then fails for the internal short circuit, while the Zn@Chelex-Zn//Cu@Chelex-Zn half cell demonstrates an average coulomb efficiency (CE) of 99.60 % in 700 cycles due to the desolvation of Chelex-Zn. Encouragingly, with the synergistic regulation of Chelex-In layer, the Zn@Chelex-In//Cu@Chelex-In half cell delivers an exceptionally high average CE of 99.85 % over 4500 stable cycles.

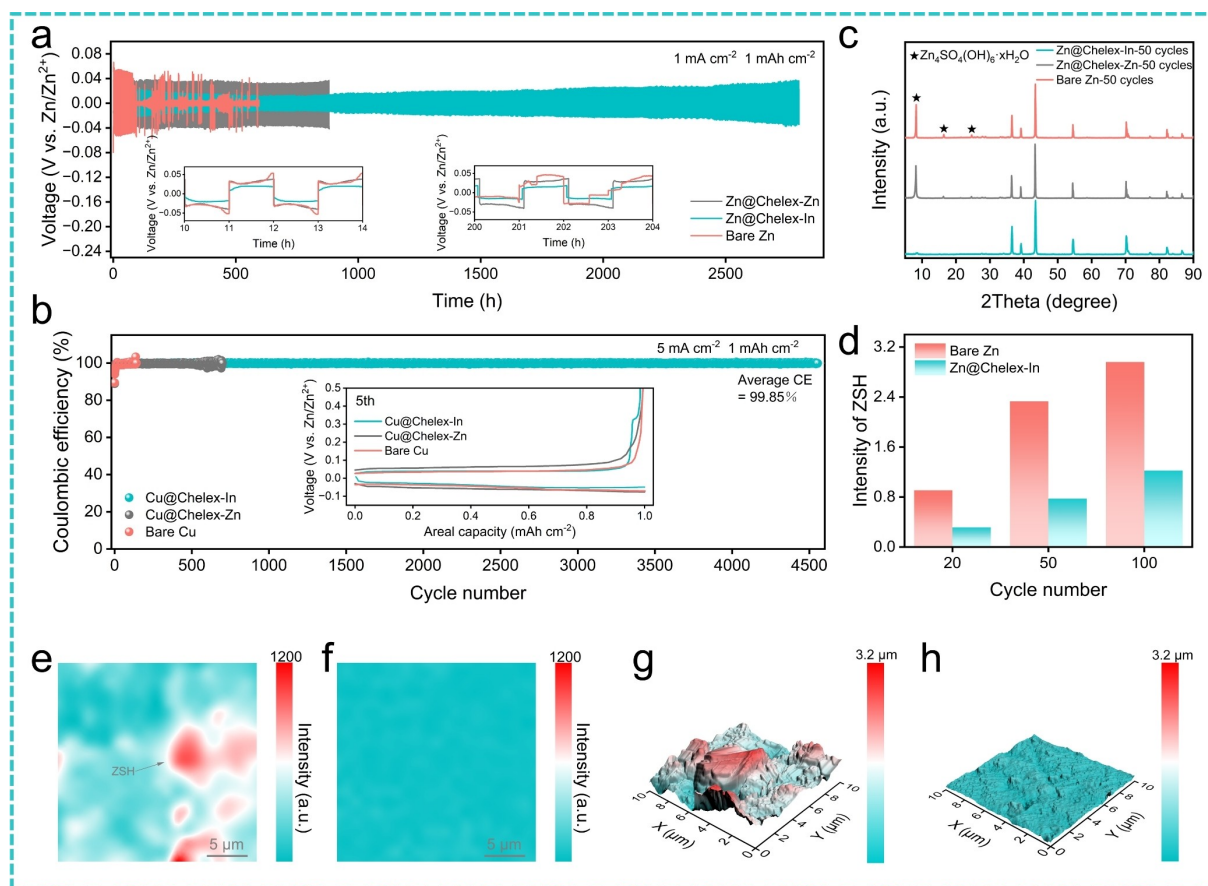


Figure 4. (a) The cycling performance of symmetric cells with different electrodes. (b) The Coulombic efficiency of different Zn//Cu half cells (insertion are the corresponding 5th capacity-voltage curves). (c) XRD patterns of different cycled electrodes. (d) The ZSH content in electrodes after different cycles obtained by ion chromatography. (e–f) Raman mapping of ZSH on the cycled (e) bare Zn and (f) Zn@Chelex-In (the resin layer is removed). (g–h) 3D superficial morphology of cycled (g) bare Zn and (h) Zn@Chelex-In (the resin layer is removed) obtained by AFM. The cycled electrodes aforementioned are all cycled at 1 mA cm⁻², 1 mAh cm⁻² for 50 times.

Besides, a new small platform emerges at 0.33 V (vs. Zn²⁺/Zn) in the capacity-voltage curve, which accounts for about 1% of the total deposition, corresponding to the dissolution process of deposited indium.

In fact, the accumulation of insulating by-products ZSH which is associated with the HER side reaction, is one of the culprits for zinc anode deterioration, since the insulating ZSH will cover the active site for electrodeposition, exacerbating the surface inhomogeneity and preventing the normal deposition.^[15,30] Benefitting from the stabilized Zn/electrolyte interphase, in situ differential electrochemical mass spectroscopy (Figure S11) indicates the hydrogen evolution rate in Zn//Zn symmetric cell is significantly reduced. As depicted in Figure 4c, the emergence of new peaks at 8.2° and 16.1° in the X-ray diffraction (XRD) patterns of cycled bare Zn and Zn@Chelex-Zn indicates the accumulation of ZSH. By contrast, the peak intensity of ZSH is significantly reduced on the Zn@Chelex-In. Besides, ZSH content in deposits is quantified by ion chromatography (Figure 4d), which also reveals that the ZSH decreases markedly due to the synergistic regulation of Chelex-In layer. In addition, based on the characteristic Raman peak of ZSH at 967 cm⁻¹ (Figure S12),^[10c] the

distribution of ZSH is obtained by the Raman mapping. As shown in Figure 4e, obvious and unevenly distributed ZSH is detected on the surface of cycled bare Zn, which increases the inhomogeneity of surface and causes random Zn deposition. The atomic force microscope (AFM, Figure 4g) manifests the huge surface fluctuation of cycled bare Zn reaching several microns. Conversely, with the protection of Chelex-In layer, the ZSH is almost undetectable on the cycled Zn@Chelex-In (Figure 4f), whose surface fluctuates within a few hundred nanometers (Figure 4h), demonstrating the robust inhibitory effect on inhibiting the accumulation of by-products and dendrite growth. Above all, at the Zn electrode side, the sustainably released indium could suppress the HER and provide heterogeneous nucleation sites continuously for zinc deposition. Meanwhile, the remaining functional resin matrix enables the desolvation effect and uniform Zn²⁺ flux, relieving the corrosion from electrolytes. The synergistic regulation of Chelex-In stabilizes both the electrode and electrolyte side of interphasial region, resulting in slower side reactions and dendrite growth, improving the cyclic stability of the Zn anode.

Application of High-loading Zn//V₂O₅ Full Cells

In order to evaluate the practicability of the Chelex-In protective layer, V₂O₅ electrodes with high loading mass are used in full cell configurations. As presented in Figure 5a, the Zn@Chelex-In//V₂O₅ full cell with a high V₂O₅ loading mass of 7 mg cm⁻² can deliver an average capacity of 1.86 mAh cm⁻² for over 1300 stable cycles at a current density of 35 mA cm⁻². Peculiarly, the capacity of bare Zn//V₂O₅ full cell rapidly declines to 0 after just 120 cycles, presenting a deviation from previous findings that Zn//V₂O₅ full cells with low areal capacity could sustain prolonged cycling.^[31] The time-voltage curve (Figure 5b) reveals a sudden voltage drop during charging (corresponding to zinc deposition at the anode side), indicative of an internal short circuit caused by dendrite growth on the anode. Examination of the cycled Zn electrode shows obvious black dotted zinc deposits mixed with a yellow substance (inset of Figure 5a). The SEM and corresponding element mapping demonstrate that its surface is extensively covered by

numerous granular sediments (Figure S13), in which the element ratio of vanadium reaches as high as 23.85% (Figure S14), implying that vanadium species dissolved from the V₂O₅ cathode to the bulk electrolyte have a negative effect on the cycling performance of Zn anode in full cells. To confirm that the failure of Zn//V₂O₅ full cells is mainly due to the dendrite growth on anode, the V₂O₅ cathode recycled from the failed Zn//V₂O₅ full cell is used to reassemble batteries with the replacement of new anode, electrolyte and separator. The ICP-OES results (Table S3) indicate that 4% of the V₂O₅ is dissolved and deposited in the separator and anode. As shown in Figure S15, the capacity and voltage curve basically recover to the normal state before failure, indicating the cathode remains intact. And many metallic fragments, typical forms of dendrites that can penetrate the separator and cause internal short circuits, were even found on the cathode-facing side of the replaced separator (Figure S16). Moreover, under the more severe test condition with an extremely high loading mass of 12.24 mg cm⁻², a lower current density of 12.24 mA cm⁻², and

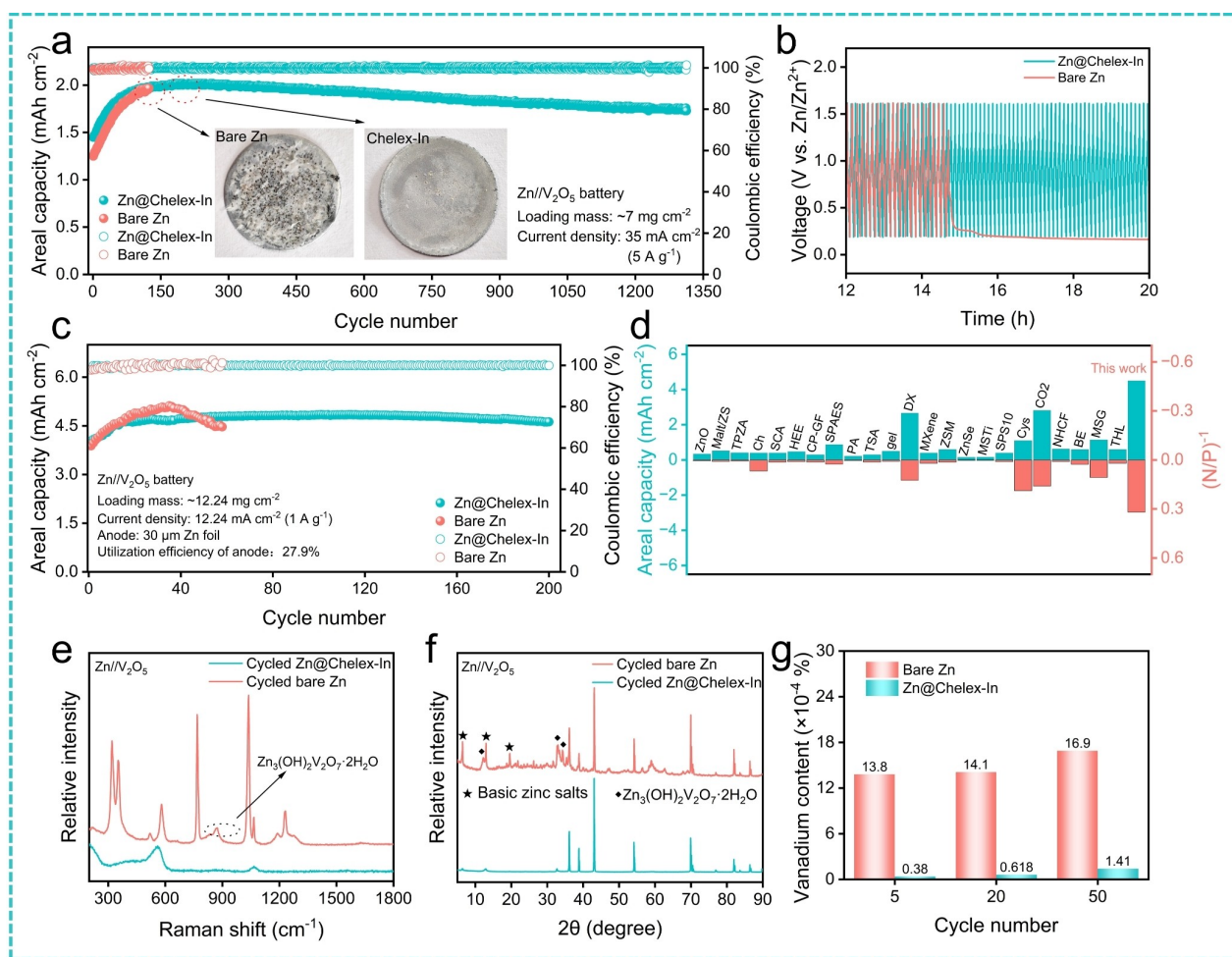


Figure 5. (a) The cyclic performance of different high-loading Zn//V₂O₅ full cells at 35 mA cm⁻² (insertion is the corresponding digital photographs of cycled electrodes) and (b) the corresponding time-voltage curve. (c) The cycling performance of different higher-loading Zn//V₂O₅ full cells under a more severe test condition, and (d) its performance in comparison with other full cells employing vanadium oxide cathodes in reported literature. (e) Raman spectra and (f) XRD spectra of cycled Zn electrodes (after 50 cycles in full cells at 5 A g⁻¹). (g) The content of vanadium in cycled Zn electrodes tested by ICP-OES.

a limited N/P ratio of 3.08, the bare Zn/V₂O₅ full cell fails rapidly within just 50 cycles (Figure 5c). By comparison, the Zn@Chelex-In/V₂O₅ cell can deliver an exceptionally high areal capacity of exceeding 4.79 mAhcm⁻² for 200 cycles, and the utilization efficiency of anode reaches 27.9%, demonstrating superior performance compared to the most recently reported Zn/V₂O₅ full cells (Figure 5d, Table S4). Even at an ultralow current density of 0.55 mAcm⁻² (50 mA g⁻¹, Figure S17), the Zn@Chelex-In/V₂O₅ full cell delivers an average capacity of exceeding 4.9 mAhcm⁻² for 10 cycles (200 h), and the utilization efficiency of anode reaches impressive 87.6% (10 μm Zn foil). Besides, the Zn@Chelex-In/V₂O₅ pouch cell can deliver an average capacity of exceeding 30 mAh, and lights the LED panel easily (Figure S18), indicating the reliability and the practical application potential of Chelex-In protective layer on Zn anode.

In order to preliminarily explore the cause of the accelerated degradation of Zn anode in full cells, cycled Zn anodes are extracted and subjected to Raman and XRD analyses. The findings, illustrated in Figure 5e and f, reveal the presence of hydrated zinc vanadate (Zn₃(OH)₂V₂O₇, ZVO) on the cycled bare Zn electrodes, whereas no significant traces of ZVO were detected on the cycled Zn@Chelex-In electrodes. Furthermore, ICP-OES results (Figure 5g) show a substantial presence of vanadium in the bare Zn after just 5 cycles, with vanadium levels increasing progressively with continued cycling. In contrast, the presence of the protective Chelex-In layer significantly curtailed the accumulation of vanadium. These preliminary investigations suggest that the persistent formation of ZVO on the Zn anode surface might be a key factor in accelerating anode degradation in full cells. The Chelex-In resin layer, by averting the formation of ZVO, potentially enhances the cyclic stability of Zn anodes, presenting an effective strategy for improving the longevity and reliability of Zn anodes in full cell configurations.

Investigation of The Zn Deterioration Induced by V₂O₅ Cathode

It is crucial to clarify the intrinsic dissolving mechanisms of vanadium species from cathode, transferring pathways in the electrolyte, and irreversible deposition behavior on Zn anode. It is well known that vanadium oxide is very sensitive to the pH of aqueous electrolytes.^[32] Given that, an acid-base titration combined with Raman spectral analysis is performed to ascertain the composition of vanadium species under varying pH conditions (Figure 6a). In detail, 1 g V₂O₅ is dispersed in 150 mL deionized water with the pH monitoring simultaneously. Then 1 M KOH is added until the pH reaching 12.59, followed by the dropwise addition of 0.5 M H₂SO₄ to adjust the pH back. As shown in Figure 6b, with the addition of KOH, the V₂O₅ gradually dissolves completely, alongside the color of the solution becomes lighter until colorless. A platform emerges at pH ≈ 6.06–6.24, corresponding to the predominant dissolution process of V₂O₅, in which the Raman spectroscopy indicates that the main species are V₂O₆(OH)³⁻ (at 949 cm⁻¹) and VO₃(OH)²⁻

(at 326 cm⁻¹).^[32c] As the pH increases, the dissolved vanadium species predominantly transitions to V₂O₇⁴⁻ (pH = 10.53, located at 877 cm⁻¹). Following acidification, the solution becomes deep yellow, and the Raman spectrum indicates the presence of V₁₀O₂₆(OH)₂⁴⁻ (pH = 4.66, located at 1005 cm⁻¹).^[32c,d] However, further acidification to a pH of 1.68 resulted in an unstable solution and gradual formation of solid vanadium oxides (Figure S19). These observations are basically consistent with the V(V)-H₂O Pourbaix diagram (Figure S20), suggesting that V₂O₅ exhibits relative stability under acidic conditions but dissolves into polyoxovanadate ions in alkaline environments. The condensation degree of these ions increases with decreasing pH and rising concentration, leading to darker coloration and more complex compositions of the solution.^[33]

It is worth noting that some polyoxovanadate ions cannot coexist with Zn²⁺ due to the pH window of Zn²⁺-containing solution and the generation of insoluble zinc vanadate. The vanadate-containing solution obtained during titration at a pH of 4.66 is mixed with the 0.5 M ZnSO₄ in a volume ratio of 1:8, thus obtaining a mixed solution (denoted as Z–V solution) containing both Zn²⁺ and vanadate. The polyoxovanadate ions with a low degree of condensation are hardly detected in Z–V solution by Raman spectra (Figure 6c). However, the Z–V solution appears as a clear yellow liquid in its digital photograph (Figure S21), indicating the existence of polyoxovanadate ions in the electrolyte.^[33b] As shown in the nuclear magnetic resonance spectrum of Z–V solution (Figure S22), the strongest peak at 515.8 ppm is assigned to the V₁₀O₂₆(OH)₂⁴⁻, and two peaks located at 499.4 ppm and 422.4 ppm are assigned to V₁₀O₂₈⁶⁻.^[32c] According to the V(V)-H₂O Pourbaix diagram, the present polyoxovanadate ion is speculated to be decavanadate (principally of V₁₀O₂₆(OH)₂⁴⁻). Since there is no insoluble matter precipitating from the Z–V solution (Figure S21), it can be proved that the Zn²⁺ can coexist with V₁₀O₂₆(OH)₂⁴⁻. After undergoing 5 cycles in a symmetric cell using Z–V solution (1 mAcm⁻², 1 mAhcm⁻²), a new Raman peak located at 877 cm⁻¹ is detected on the surface of bare Zn electrode (Figure 6c), whose location is consistent with the peak of V₂O₇⁴⁻ (pH = 10.53). Besides, this peak still exists when the Z–V solution is added onto the cycled Zn electrode (Figure 6c), confirming the emergence of the newly formed vanadium-containing insoluble species (Zn₃(OH)₂V₂O₇·2H₂O, ZVO),^[32c,d] showing the complex interactions between vanadium species and electrolyte environment.

In situ Raman spectroscopy was employed within a symmetric cell utilizing the Z–V solution to explore the formation mechanisms of ZVO on Zn anodes. As shown in Figure 6d, shortly after the beginning of electrodeposition, a distinct peak of ZSH (967 cm⁻¹) appears on the surface of bare Zn, which can be attributed to the pH increase at the interface of Zn/electrolyte. Subsequently, the peak of ZVO is observed at 877 cm⁻¹ and exhibits a low intensity during the early stages of deposition. As zinc is stripped in the subsequent process, the intensity of ZVO peak increases, indicating the persistence of ZVO. However, by the second cycle, the ZVO peak vanishes, likely due to the overlay of

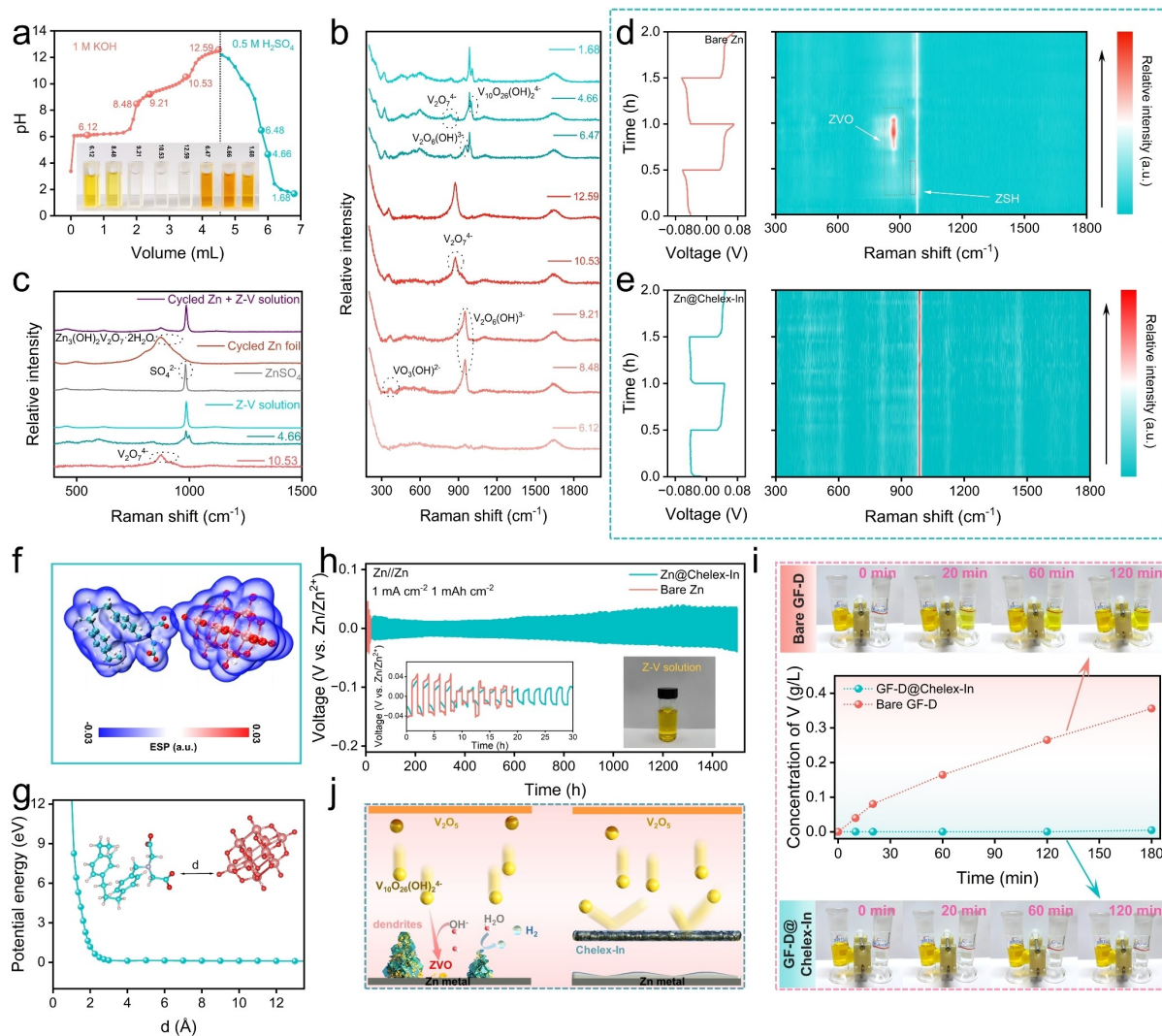
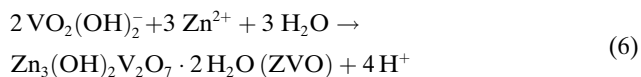
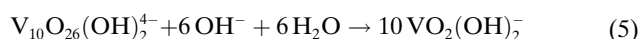
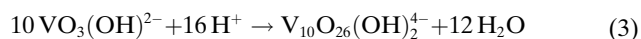
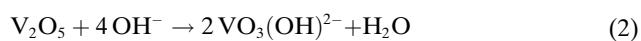


Figure 6. (a) Acid-base titration curve of V_2O_5 by 1 M KOH and 0.5 M H_2SO_4 (the insertion is digital photos of solutions at different pH conditions), and (b) their corresponding Raman spectra. (c) Raman spectra of different solutions and cycled Zn foil. (d–e) In situ Raman spectra of (d) bare Zn and (e) Zn@Chelex-In electrodes in Z–V solution, which are performed in symmetric cells at 5 mA cm^{-2} for 2.5 mAh cm^{-2} . (f) The ESP isosurface plots between Chelex and $V_{10}O_{26}(\text{OH})_2^{4-}$. (g) The potential energy of IDA group in Chelex interacting with $V_{10}O_{26}(\text{OH})_2^{4-}$ ion. (h) The cycle performance of symmetric cells with Z–V solution ($ZnSO_4$ is 2 M) electrolyte. (i) The diffusion test of soluble vanadium species performed in an H-type electrolytic cell (the solution is obtained from the acid-base titration process at pH of 4.66), and the corresponding concentration of vanadium obtained by ICP-OES. (j) Schematic diagram of deterioration for bare Zn anode in Zn// V_2O_5 full cells and the protection mechanism of the Chelex-In layer.

extensive dendritic growth (Figure S23). Notably, the emergence of ZVO leads to the consumption of OH^- , competing with the formation of ZSH, which disappears upon ZVO formation. Moreover, according to the in situ Raman spectra performed in pure 0.5 M $ZnSO_4$ electrolyte (Figure S24), it is observed that only the ZSH appears repeatedly during the cycling, while there is no change observed at around 877 cm^{-1} , confirming the extra peak observed in the above mentioned Z–V solution is indeed related to the insoluble vanadium species. The configurations of vanadium compounds are determined by the concentration of vanadium and the pH of solution.^[32e,34] Accordingly, it can be speculated that the vanadium species in full cells with high-loading of V_2O_5 undergo the following steps to generate

ZVO on the zinc anode: During the discharging process, the proton-embedding leads to a localized increase in pH at the cathode interface, which leads to the dissolution of V_2O_5 (Figure S25, equation 2).^[32d,e,35] Subsequently, the dissolved vanadium species will be exposed to the bulk electrolyte and suffer from the pH decrease, thus part of them are transformed into $V_{10}O_{26}(\text{OH})_2^{4-}$ (equation 3),^[32d,36] and shuttles towards the anode side. The HER side reaction on zinc anode will result in the pH increase at the Zn/electrolyte (equation 4),^[30] leading to the formation of vanadium species with a lower degree of condensation (equation 5),^[33] which will combine with Zn^{2+} to generate the insoluble ZVO (equation 6).^[32b]



Encouragingly, with the protection of Chelex-In resin layer, neither ZSH nor ZVO are detected throughout the entire cycling process (Figure 6e). Moreover, the Raman characteristic peak of Chelex-In remains unaltered (Figure S26), proving the excellent chemical stability of Chelex-In. Furthermore, theoretical simulations are performed to investigate how the Chelex-In layer prevents the migration of soluble vanadium species. As presented in the ESP results (Figure 6f), the richness of negative charge in Chelex can keep the decavanadate away from the layer. Besides, the potential energy between the IDA group and decavanadate is always positive (Figure 6g), demonstrating that Chelex is capable of repelling detrimental decavanadate ions, thus helping to prevent the formation of ZVO on the anode surface. In a further step, the Z–V solution (containing 2 M ZnSO_4) is directly employed as the electrolyte for Zn//Zn symmetric cells to evaluate its influence on the zinc anode. With the introduction of soluble vanadium species, the bare Zn//Z–V solution//Zn symmetric cell fails within less than 5 cycles due to the internal short circuit (Figure 6h), whose lifespan is much shorter than the symmetric cell employing pure ZnSO_4 electrolyte (80 h, Figure 4a), highlighting the serious damage caused by ZVO accumulation. However, with the protection of Chelex-In layer, the lifespan of the symmetric cell is extended to 1500 h, which proves the reliability of the Chelex-In layer in preventing the erosion from vanadium species. Besides, an intuitive diffusion test is conducted in the H-type electrolytic cells (Figure 6i), which validates that the Chelex-In resin layer can significantly impede the shuttle of soluble vanadium species. The richness of immobilized anion in Chelex-In resin can prevent the decavanadate anion in electrolyte from contacting with zinc anode directly through the electrostatic repulsion, meanwhile its synergistic regulation can inhibit the side reaction and mitigates the pH fluctuations on the anode, thereby averting ZVO generation on zinc electrode (Figure 6j). In addition, the iodide cathode, which also suffers from the serious crosstalk of dissolved cathode species (shuttle effect of anionic polyiodide intermediates),^[37] was also employed as the cathode for the full cell assembly. As presented in Figure S27, the Chelex-In layer can effectively inhibit the shuttle of polyiodide, stabilizing the Zn anode. And the Zn@Chelex-In//I₂ full cell can deliver an average discharge capacity of 2.36 mAh cm⁻² for exceeding 250 cycles with an ultralow N/P ratio of 1.34, proving practical potential and universality of indium-chelated resin protective layer.

Conclusion

To conclude, from the perspective of stabilizing both the Zn metal phase and the electrolyte phase of the Zn electrode/electrolyte interphasial region, an indium-chelated resin layer is developed on Zn surface to ensure the reversible Zn chemistry throughout the entire lifespan. On the electrode surface, the sustained indium release enables the persistent anticatalytic effect of HER and continuous heterogeneous nucleation sites for Zn deposition. In the electrolyte phase, the anion-immobilized resin matrix can coordinate with zinc ions and repel the injurious ingredients to achieve slower side reactions and uniform Zn^{2+} flux. Moreover, given the huge discrepancy in Zn-anode's lifespan in symmetrical cells compared to that in full cells, this work proves the dissolved cathode species, such as the decavanadate anions from V_2O_5 cathode, is the primary factor that accelerates the deterioration of Zn, particularly in the high-areal-capacity conditions. Accordingly, based on preventing the crosstalk of anionic cathode-dissolve products, such ingenious design of chelated-resin modification reconciles Zn nucleation and mass transfer behavior in the Zn/electrolyte interphasial region, providing new insights into the practical high-areal-capacity zinc metal batteries.

Acknowledgements

M.H. Zhang and S.Y. Li contributed equally to this work. The authors gratefully acknowledge the financial support from National Natural Science Foundation of China (No. 22379125, 22109030, 52271204, and 22021001), Fundamental Research Funds for the Central Universities (20720220073), The Key Research and Development Program of Yunnan Province (202103AA080019), Fujian Industrial Technology Development and Application Plan (2022I0002). The authors acknowledge Wenhao, Yang and Prof. Xue Li from Kunming University of Science and Technology for the DEMS tests. The authors acknowledge Tan Kah Kee Innovation Laboratory for the help of scientific tests. The numerical calculations in this paper have been done on Hefei advanced computing center.

Conflict of Interest

The authors declare no conflict of interest.

Data Availability Statement

The data that support the findings of this study are available from the corresponding author upon reasonable request.

Keywords: chelated resin · sustained indium release · Zn/electrolyte interphase · heterogeneous nucleation · cathode dissolution

- [1] a) B. Dunn, H. Kamath, J. M. Tarascon, *Science* **2011**, *334*, 928–935; b) Z. Yang, J. Zhang, M. C. W. Kintner-Meyer, X. Lu, D. Choi, J. P. Lemmon, J. Liu, *Chem. Rev.* **2011**, *111*, 3577–3613; c) M. D. Leonard, E. E. Michaelides, D. N. Michaelides, *Renewable Energy* **2020**, *145*, 951–962.
- [2] a) H. Tian, Z. Li, G. Feng, Z. Yang, D. Fox, M. Wang, H. Zhou, L. Zhai, A. Kushima, Y. Du, Z. Feng, X. Shan, Y. Yang, *Nat. Commun.* **2021**, *12*, 237; b) L. K. Zhao, X. W. Gao, J. Mu, W. B. Luo, Z. Liu, Z. Sun, Q. F. Gu, F. Li, *Adv. Funct. Mater.* **2023**, *33*, 2304292.
- [3] a) L. Lin, Z. Lin, J. Zhu, K. Wang, W. Wu, T. Qiu, X. Sun, *Energy Environ. Sci.* **2023**, *16*, 89–96; b) C. Li, S. Jin, L. A. Archer, L. F. Nazar, *Joule* **2022**, *6*, 1733–1738; c) S. W. D. Gourley, R. Brown, B. D. Adams, D. Higgins, *Joule* **2023**, *7*, 1415–1436; d) T. Wang, S. Li, X. Weng, L. Gao, Y. Yan, N. Zhang, X. Qu, L. Jiao, Y. Liu, *Adv. Energy Mater.* **2023**, *13*, 2204358.
- [4] a) S. Zheng, L. Wei, Z. Zhang, J. Pan, J. He, L. Gao, C. C. Li, *Nano Lett.* **2022**, *22*, 9062–9070; b) Y. Song, P. Ruan, C. Mao, Y. Chang, L. Wang, L. Dai, P. Zhou, B. Lu, J. Zhou, Z. He, *Nano-Micro Lett.* **2022**, *14*, 218; c) D. Wang, Z. Liu, X.-W. Gao, Q. Gu, L. Zhao, W.-B. Luo, *J. Energy Storage* **2023**, *72*, 108740.
- [5] a) S. Trasatti, R. Parsons, *Pure Appl. Chem.* **1986**, *58*, 437–454; b) L. Ma, T. P. Pollard, M. A. Schroeder, C. Luo, Y. Zhang, G. Pastel, L. Cao, J. Zhang, V. Shipitsyn, Y. Yao, C. Wang, O. Borodin, K. Xu, *Energy Environ. Sci.* **2024**, *17*, 2468–2479.
- [6] a) Z. Meng, Y. Jiao, P. Wu, *Angew. Chem. Int. Ed.* **2023**, *62*, e202307271; b) Y. Wang, T. Wang, S. Bu, J. Zhu, Y. Wang, R. Zhang, H. Hong, W. Zhang, J. Fan, C. Zhi, *Nat. Commun.* **2023**, *14*, 1828; c) X. Yu, Z. Li, X. Wu, H. Zhang, Q. Zhao, H. Liang, H. Wang, D. Chao, F. Wang, Y. Qiao, H. Zhou, S.-G. Sun, *Joule* **2023**, *7*, 1145–1175; d) W. Du, J. Yan, C. Cao, C. C. Li, *Energy Storage Mater.* **2022**, *52*, 329–354.
- [7] a) F. Wang, J. Zhang, H. Lu, H. Zhu, Z. Chen, L. Wang, J. Yu, C. You, W. Li, J. Song, Z. Weng, C. Yang, Q.-H. Yang, *Nat. Commun.* **2023**, *14*, 4211; b) S. Chen, Y. Ying, L. Ma, D. Zhu, H. Huang, L. Song, C. Zhi, *Nat. Commun.* **2023**, *14*, 2925.
- [8] a) J. Ke, Z. Wen, Y. Yang, R. Tang, Y. Tang, M. Ye, X. Liu, Y. Zhang, C. C. Li, *Adv. Funct. Mater.* **2023**, *33*, 2301129; b) F. Yang, J. A. Yuwono, J. Hao, J. Long, L. Yuan, Y. Wang, S. Liu, Y. Fan, S. Zhao, K. Davey, Z. Guo, *Adv. Mater.* **2022**, *34*, 2206754; c) W. Yang, X. Du, J. Zhao, Z. Chen, J. Li, J. Xie, Y. Zhang, Z. Cui, Q. Kong, Z. Zhao, C. Wang, Q. Zhang, G. Cui, *Joule* **2020**, *4*, 1557–1574; d) F. Ling, L. Wang, F. Liu, M. Ma, S. Zhang, X. Rui, Y. Shao, Y. Yang, S. He, H. Pan, X. Wu, Y. Yao, Y. Yu, *Adv. Mater.* **2023**, *35*, 2208764; e) M. Liu, W. Yuan, G. Ma, K. Qiu, X. Nie, Y. Liu, S. Shen, N. Zhang, *Angew. Chem. Int. Ed.* **2023**, *62*, e202304444.
- [9] Y. Deng, H. Wang, M. Fan, B. Zhan, L.-J. Zuo, C. Chen, L. Yan, *J. Am. Chem. Soc.* **2023**, *145*, 20109–20120.
- [10] a) J. Hao, B. Li, X. Li, X. Zeng, S. Zhang, F. Yang, S. Liu, D. Li, C. Wu, Z. Guo, *Adv. Mater.* **2020**, *32*, 2003021; b) Y. Yang, C. Liu, Z. Lv, H. Yang, Y. Zhang, M. Ye, L. Chen, J. Zhao, C. C. Li, *Adv. Mater.* **2021**, *33*, 2007388; c) Z. Zhao, R. Wang, C. Peng, W. Chen, T. Wu, B. Hu, W. Weng, Y. Yao, J. Zeng, Z. Chen, P. Liu, Y. Liu, G. Li, J. Guo, H. Lu, Z. Guo, *Nat. Commun.* **2021**, *12*, 6606; d) J. Zhu, Z. Bie, X. Cai, Z. Jiao, Z. Wang, J. Tao, W. Song, H. J. Fan, *Adv. Mater.* **2022**, *34*, 2207209; e) Y. Meng, M. Wang, J. Xu, K. Xu, K. Zhang, Z. Xie, Z. Zhu, W. Wang, P. Gao, X. Li, W. Chen, *Angew. Chem. Int. Ed.* **2023**, *62*, e202308454.
- [11] a) D. Wang, H. Liu, D. Lv, C. Wang, J. Yang, Y. Qian, *Adv. Mater.* **2023**, *35*, 2207908; b) M. Y. Abyaneh, *J. Electrochem. Soc.* **2018**, *165*, D142–D146.
- [12] a) M. Kim, J. Lee, Y. Kim, Y. Park, H. Kim, J. W. Choi, *J. Am. Chem. Soc.* **2023**, *145*, 15776–15787; b) M. Tomellini, *Physica A* **2020**, *558*, 124981; c) M. Y. Abyaneh, *J. Electrochem. Soc.* **2020**, *167*, 132506.
- [13] a) Z. Zhao, Y. He, W. Yu, W. Shang, Y. Ma, P. Tan, *Proc. Natl. Acad. Sci. USA* **2023**, *120*, e2307847120; b) Y. Zou, X. Yang, L. Shen, Y. Su, Z. Chen, X. Gao, J. Zhou, J. Sun, *Energy Environ. Sci.* **2022**, *15*, 5017–5038; c) Z. Yang, C. Hu, Q. Zhang, T. Wu, C. Xie, H. Wang, Y. Tang, X. Ji, H. Wang, *Angew. Chem. Int. Ed.* **2023**, *62*, e202308017.
- [14] a) F. Xie, H. Li, X. Wang, X. Zhi, D. Chao, K. Davey, S. Z. Qiao, *Adv. Energy Mater.* **2021**, *11*, 2003419; b) Y. Dai, C. Zhang, W. Zhang, L. Cui, C. Ye, X. Hong, J. Li, R. Chen, W. Zong, X. Gao, J. Zhu, P. Jiang, Q. An, D. J. L. Brett, I. P. Parkin, G. He, L. Mai, *Angew. Chem. Int. Ed.* **2023**, *62*, e202301192; c) B. Li, K. Yang, J. Ma, P. Shi, L. Chen, C. Chen, X. Hong, X. Cheng, M. C. Tang, Y. B. He, F. Kang, *Angew. Chem. Int. Ed.* **2022**, *61*, e202212587; d) J. Zheng, X. Liu, Y. Zheng, A. N. Gandi, X. Kuai, Z. Wang, Y. Zhu, Z. Zhuang, H. Liang, *Nano Lett.* **2023**, *23*, 6156–6163; e) L. Wang, W. Huang, W. Guo, Z. H. Guo, C. Chang, L. Gao, X. Pu, *Adv. Funct. Mater.* **2021**, *32*, 2108533; f) R. Zhao, X. Dong, P. Liang, H. Li, T. Zhang, W. Zhou, B. Wang, Z. Yang, X. Wang, L. Wang, Z. Sun, F. Bu, Z. Zhao, W. Li, D. Zhao, D. Chao, *Adv. Mater.* **2023**, *35*, 2209288; g) X. Zheng, Z. Liu, J. Sun, R. Luo, K. Xu, M. Si, J. Kang, Y. Yuan, S. Liu, T. Ahmad, T. Jiang, N. Chen, M. Wang, Y. Xu, M. Chuai, Z. Zhu, Q. Peng, Y. Meng, K. Zhang, W. Wang, W. Chen, *Nat. Commun.* **2023**, *14*, 76.
- [15] L. Yuan, J. Hao, C.-C. Kao, C. Wu, H.-K. Liu, S.-X. Dou, S.-Z. Qiao, *Energy Environ. Sci.* **2021**, *14*, 5669–5689.
- [16] X. Ji, L. F. Nazar, *Nat. Sustain.* **2024**, *7*, 98–99.
- [17] a) N. Manouchehri, A. Bermond, *Anal. Chim. Acta* **2006**, *557*, 337–343; b) N. I. Gorshkov, A. E. Miroslavov, I. E. Alekseev, A. A. Lumpov, A. Y. Murko, I. I. Gavrilova, N. N. Saprykina, M. A. Bezrukova, A. I. Kipper, V. D. Krasikov, D. N. Suglobov, M. Y. Tyupina, E. F. Panarin, *J. Labelled Compd. Radiopharm.* **2017**, *60*, 302–311.
- [18] a) R. Shibahara, K. Kamiya, Y. Nishina, *Nanoscale Adv.* **2021**, *3*, 5823–5829; b) L. Wang, X. Xu, D. G. Evans, X. Duan, D. Li, *J. Solid State Chem.* **2010**, *183*, 1114–1119.
- [19] a) C.-P. Chen, D.-Y. Lee, K.-W. Juang, T.-H. Lin, *Soil Sci.* **2008**, *173*, 638–648; b) S. Acharya, N. Gaowa, H. Ohashi, D. Kawamoto, T. Honma, Y. Okaue, T. Yokoyama, *Bull. Chem. Soc. Jpn.* **2017**, *90*, 1372–1374; c) R. A. Fischer, J. Weiß, *Angew. Chem. Int. Ed.* **1999**, *38*, 2830–2850.
- [20] C. Zhen, S. Sun, C. Fan, S. Chen, B. Mao, Y. Fan, *Electrochim. Acta* **2004**, *49*, 1249–1255.
- [21] L. Jiang, D. Li, X. Xie, D. Ji, L. Li, L. Li, Z. He, B. Lu, S. Liang, J. Zhou, *Energy Storage Mater.* **2023**, *62*, 102932.
- [22] H. B. Dong, X. Y. Hu, R. R. Liu, M. Z. Ouyang, H. Z. He, T. L. Wang, X. Gao, Y. H. Dai, W. Zhang, Y. Y. Liu, Y. Q. Zhou, D. J. L. Brett, I. P. Parkin, P. R. Shearing, G. J. He, *Angew. Chem. Int. Ed.* **2023**, *62*, e202311268.
- [23] J. Hao, L. Yuan, C. Ye, D. Chao, K. Davey, Z. Guo, S. Z. Qiao, *Angew. Chem. Int. Ed.* **2021**, *60*, 7366–7375.
- [24] Y. Yang, H. Hua, Z. Lv, W. Meng, M. Zhang, H. Li, P. Lin, J. Yang, G. Chen, Y. Kang, Z. Wen, J. Zhao, C. C. Li, *ACS Energy Lett.* **2023**, 1959–1968.
- [25] T. T. Yang, W. A. Saidi, *J. Phys. Chem. Lett.* **2022**, *13*, 5310–5315.
- [26] J. Mu, Z. Zhao, X. W. Gao, Z. M. Liu, W. B. Luo, Z. Sun, Q. F. Gu, F. Li, *Adv. Energy Mater.* **2023**, 2303558.
- [27] J. X. Zheng, Q. Zhao, T. Tang, J. F. Yin, C. D. Quilty, G. D. Renderos, X. T. Liu, Y. Deng, L. Wang, D. C. Bock, C. Jaye, D. H. Zhang, E. S. Takeuchi, K. J. Takeuchi, A. C. Marschilok, L. A. Archer, *Science* **2019**, *366*, 645–648.

- [28] F. Li, D. Ma, K. Ouyang, M. Yang, J. Qiu, J. Feng, Y. Wang, H. Mi, S. Sun, L. Sun, C. He, P. Zhang, *Adv. Energy Mater.* **2023**, *13*, 2204365.
- [29] a) P. Xiao, H. Li, J. Fu, C. Zeng, Y. Zhao, T. Zhai, H. Li, *Energy Environ. Sci.* **2022**, *15*, 1638–1646; b) M. Fayette, H. J. Chang, X. Li, D. Reed, *ACS Energy Lett.* **2022**, *7*, 1888–1895.
- [30] M. Zhang, H. Hua, P. Dai, Z. He, L. Han, P. Tang, J. Yang, P. Lin, Y. Zhang, D. Zhan, J. Chen, Y. Qiao, C. C. Li, J. Zhao, Y. Yang, *Adv. Mater.* **2023**, *35*, 2208630.
- [31] a) S. Liu, J. Mao, W. K. Pang, J. Vongsvivut, X. Zeng, L. Thomsen, Y. Wang, J. Liu, D. Li, Z. Guo, *Adv. Funct. Mater.* **2021**, *31*, 2104281; b) Y. Zhu, H. Y. Hoh, S. Qian, C. Sun, Z. Wu, Z. Huang, L. Wang, M. Batmunkh, C. Lai, S. Zhang, Y. L. Zhong, *ACS Nano* **2022**, *16*, 14600–14610; c) D. Yuan, X. Li, H. Yao, Y. Li, X. Zhu, J. Zhao, H. Zhang, Y. Zhang, E. T. J. Jie, Y. Cai, M. Srinivasan, *Adv. Sci.* **2023**, *10*, 2206469.
- [32] a) Z. Xing, G. Xu, J. Han, G. Chen, B. Lu, S. Liang, J. Zhou, *Trends Chem.* **2023**, *5*, 380–392; b) Y. Kim, Y. Park, M. Kim, J. Lee, K. J. Kim, J. W. Choi, *Nat. Commun.* **2022**, *13*, 2371; c) W. Wang, X. Zhang, S. Wu, B. Xu, S. Li, L. He, X. Li, Z. Chen, Y. Fan, A. L. R. Vellaisamy, *J. Raman Spectrosc.* **2020**, *51*, 2182–2191; d) K. Zhu, T. Wu, K. Huang, *Chem. Mater.* **2021**, *33*, 4089–4098; e) J. Livage, *Coord. Chem. Rev.* **1998**, *178*, 999–1018.
- [33] a) J. Livage, *Materials* **2010**, *3*, 4175–4195; b) T. Kojima, M. R. Antonio, T. Ozeki, *J. Am. Chem. Soc.* **2011**, *133*, 7248–7251.
- [34] J. L. Ferreira da Silva, M. Fátima Minas da Piedade, M. Teresa Duarte, *Inorg. Chim. Acta* **2003**, *356*, 222–242.
- [35] Q. Zhao, L. J. Liu, J. F. Yin, J. X. Zheng, D. H. Zhang, J. Chen, L. A. Archer, *Angew. Chem. Int. Ed.* **2020**, *59*, 3048–3052.
- [36] a) R. K. Murmann, K. C. Giese, *Inorg. Chem.* **1978**, *17*, 1160–1166; b) V. W. Day, W. G. Klemperer, D. J. Maltbie, *J. Am. Chem. Soc.* **1987**, *109*, 2991–3002.
- [37] a) W. Li, L. Huang, H. Zhang, Y. Wu, F. Wei, T. Zhang, J. Fu, C. Jing, J. Cheng, S. Liu, *Matter* **2023**, *6*, 2312–2323; b) H. Chen, X. Li, K. Fang, H. Wang, J. Ning, Y. Hu, *Adv. Energy Mater.* **2023**, *13*, 2302187.

Manuscript received: March 21, 2024

Accepted manuscript online: May 8, 2024

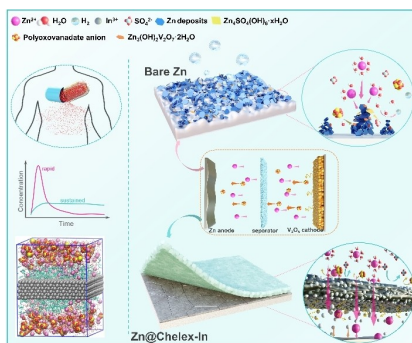
Version of record online: ■■, ■■

Research Articles

Zinc Metal Batteries

M. Zhang, S. Li, R. Tang, C. Sun, J. Yang,
G. Chen, Y. Kang, Z. Lv, Z. Wen, C. C. Li,*
J. Zhao,* Y. Yang* e202405593

Stabilizing Zn/electrolyte Interphasial
Chemistry by a Sustained-Release Drug
Inspired Indium-Chelated Resin Protective
Layer for High-Areal-Capacity Zn//V₂O₅ Bat-
teries



An indium-chelated resin protective layer is designed to stabilize the Zn/electrolyte interphasial region. The sustained release of In³⁺ can provide continuous heterogeneous nucleation sites for Zn deposition and alleviate HER side reactions, meanwhile the anchored resin matrix layer can repel detrimental anions like SO₄²⁻ and V₁₀O₂₆(OH)₂⁴⁻, circumventing serious dendrite growth.